Applied Radiation and Isotopes 231 (2026) 112485

Contents lists available at ScienceDirect

Applied Radiation and Isotopes

journal homepage: www.elsevier.com/locate/apradiso

Traceable in-situ calibration of low activity concentration radon detectors ☆

Stefan Röttger [a,*], Florian Mertes [a,b], Scott Chambers [c], Alan Griffiths [c], Roger Curcoll [d], Arturo Vargas [d], José Luis Gutiérrez Villanueva [e], Annette Röttger [a]

[a] Physikalisch-Technische Bundesanstalt (PTB), Braunschweig, Germany
[b] Bundesamt für Strahlenschtz (BfS), Germany
[c] Australian Nuclear Science and Technology Organisation (ANSTO), Australia
[d] Polytechnic University of Catalonia - Institute of Energy Technologies (UPC-INTE), Spain
[e] Radonova Laboratories, Sweden

ARTICLE INFO

Keywords:
Radon
Low-activity concentration
Tracer
Calibration
Uncertainty
In-situ
Operando
Pulse method

ABSTRACT

Radon gas is the largest source of public exposure to naturally occurring radioactivity, and concentration maps based on atmospheric measurements facilitate compliance with national implementation of the Council Directive 2013/59/Euratom. A number of different metrology projects dealing with the traceability of radon measurements for different reasons and in different conditions have been funded. As a health risk in dwellings and workplaces (MetroRADON, EMPIR), as an atmospheric tracer in a climate change mitigation context (traceRadon, EMPIR), networked in big buildings or future cities (RadonNET, EPM), and at coastal or remote oceanic island sites in a climate change monitoring context (NuClim, EURATOM). Calibrations with small uncertainties that are traceable to the Système international d'unités (SI) (The International System of Units (SI), 2019) are needed for low ^{222}Rn activity concentrations under difficult conditions. Starting with different classical calibration solutions, we then propose and explain a new in-situ operando calibration technique (the pulse calibration method), and provide two examples of these calibration techniques for research grade outdoor air activity concentration detectors.

1. Introduction

Radon gas is the largest source of public exposure to naturally occurring radioactivity, and concentration maps based on atmospheric measurements facilitate compliance with national implementation of the Council Directive 2013/59/Euratom. Furthermore, radon can be used as a tracer to evaluate the performance of atmospheric models that support successful greenhouse gas (GHG) mitigation. That is why reliable measurements of low-level radon activity concentrations, such as those found in the environment (< 20 Bq m^{-3}) are important for radiation protection, climate and air quality research. Despite the enormous changes in radon metrology in recent years, activity concentrations below 100 Bq m^{-3} had not been subject to metrological traceable calibration (SI2, 2019) research until 2020. At that time, within the framework of the EMPIR project traceRadon (traceRadon, 2019), stable atmospheres with low-level activity concentrations of radon were produced to enable calibration of radon detectors capable of measuring these environmental activity concentrations for the first time. Following this, the European Metrology Partnership funded a project in 2024, RadonNET (RadonNET, 2023), which focuses more on energy savings by smart inhouse detector networks for big buildings and future cities. Parallel to that, the project NuClim (NuClim, 2023), from a EURATOM call intends to make use of radon as a tracer of terrestrial influence on remote marine air masses for climate and air quality studies. This will require even lower activity concentration calibrations, also in place, because the associated detectors are in remote, hard to reach locations, and they are large (not readily portable) to enable the required high measurement sensitivity.

1.1. New challenges for radon metrology

The RadonNET and NuClim projects require SI traceable (SI2, 2019) in place and in-situ operando calibrations, respectively, necessitating the development of new techniques. To this end, low activity sources of radium were produced with different methods and different characteristics. Sources down to a few Bq of ^{226}Ra were developed and characterized leading to uncertainties as low as 2%.[1] Additionally, sources with

☆ This article is part of a Special issue entitled: 'ICRM 2025' published in Applied Radiation and Isotopes.

* Corresponding author.
E-mail address: Stefan.Roettger@PTB.de (S. Röttger).

[1] Unless otherwise stated, all uncertainties reported here are standard uncertainties ($k = 1$).

https://doi.org/10.1016/j.apradiso.2026.112485
Received 27 June 2025; Received in revised form 9 January 2026; Accepted 6 February 2026
Available online 14 February 2026

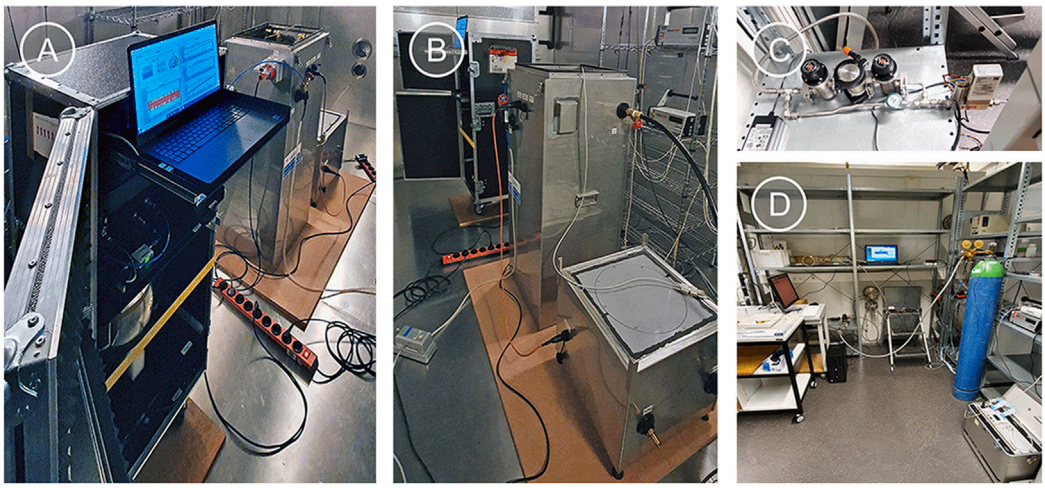

Fig. 1. Pictures of the calibration and measurement setup with the ANSTO 200 L and the ARMON v2 detectors in the PTB climate chamber. (A) shows the open box of the ARMON v2 detector in front, with the notebook and the detector sphere behind the yellow bar. (B) shows the ANSTO 200 L detector in the middle, with the thoron (^{220}Rn) delay volume in front. (C) shows the housing of the emanation source in between the valves for the build up of a defined activity and the mass flow controller for the pulse calibration. (D) shows all external climate chamber connections for the static and pulse calibrations including the canister with aged synthetic air ($200{\cdot}10^3$ hPa, 50 L) in blue with green shoulder.

advanced production methods like ion implantation of mass separated ^{226}Ra in different target materials where produced (Mertes et al., 2022). As an outcome, traceable methods for measuring low-level atmospheric radon activity concentrations in the range of 1 Bq m^{-3} to 20 Bq m^{-3} are now available with uncertainties below 5 % (Röttger et al., 2023). To apply these sources for in-situ operando calibration a new technique is investigated. The radon atmosphere is built up from ^{226}Ra sources in a separate, small volume. At the desired time of calibration, the traceable absolute activity of ^{222}Rn is flushed with a traceable flow of radon-free air through the active detector volume itself. With a model of the known detection process and associated parameters, a calibration can thus be achieved within hours instead of months (Mertes, 2023a). Repeated in-situ operando calibration will allow for stability testing and predictive maintenance procedures. The details of the calibration procedure are described, as well as the differences between spectrometric and integral counting detection principles and the uncertainties assigned to each procedure and system. Lastly, the results of the characterization of two research grade detectors are discussed.

2. Prototypes of low-level radon detectors

At PTB, a 21.035(30) m^3 ^{222}Rn-tight climate chamber is available, within which the ANSTO 200 L and the ARMON v2 ^{222}Rn detector were installed — see Fig. 1. The chamber is constructed from welded 0.6 mm stainless steel (V4 A) with 100 mm polyurethane foam insulation, yielding a heat transmission coefficient smaller than k = 0.2 W m^{-2} K^{-1} (Honig et al., 1998) and guaranties stable environmental conditions. The dimensions are (4800 ·2190 ·2500) mm^3 with an additional walkable air lock. The two detectors are research grade detectors developed to measure outdoor air activity concentration levels, see Section 2.1 or Chambers et al. (2022) and 2.2 or Curcoll et al. (2024) for more details.

The chamber has external ports, through which a specifically designed stainless steel housing can be connected. Into this housing, characterized emanation sources were installed and the generated ^{222}Rn was extracted by circulating chamber air through the housing at a nominal flow rate of 1 L min^{-1}. Consequently, the steady-state ^{222}Rn activity concentration in the chamber can be calculated from the ^{222}Rn emanation rate of the sources and the known volume of the chamber of 21.224(17) m^3, also accounting for the volume displaced by the ANSTO 200 L, the ARMON v2 and the AlphaGUARD devices. All measurement points shown in Fig. 2 represent an integration time of 1800 s for the respective device. Naturally, one observes characteristic in-growth and decay of the ^{222}Rn activity concentration and the expected ^{222}Rn decay constant is confirmed with the known uncertainties (Bé et al., 2008). Negative activity concentration values visible in Fig. 2 are due to the fact, that the calibration procedure of the devices includes subtraction of an instrumental background, with its own associated uncertainty. With these small activity concentration values and comparably large statistical fluctuations, negative values become visible. This is just statistical probability without physical meaning. A more in depth discussion is found in Section 3.

Specifically, the sources identified by their serial numbers 2018–1121, 2018–1133 and 2018–1120 and described in Mertes et al. (2022) were used as shown in Fig. 2 to generate ^{222}Rn atmospheres in the chamber, whose in-growth and decay regimes can be well described due to the stable conditions under which they take place and whose steady-state values are below ≈50 Bq m^{-3}. Within this calibration exercise the ANSTO 200 L (see Section 2.1), the ARMON v2 (see Section 2.2) and two commercial AlphaGUARD ^{222}Rn detectors were used.

2.1. ANSTO 200 L

In the hemispheric "background" atmosphere (e.g. remote marine environments or the free troposphere), radon activity concentrations are routinely below 0.1 Bq m^{-3} (Chambers et al., 2016), however, most environmental and public health radon monitoring applications (e.g. GHG emission studies using the Radon Tracer Method, atmospheric mixing and transport studies, urban climate studies, urban pollution studies, evaluation of regional and global chemical transport models, public exposure monitoring, determination of Radon Priority Areas (RPA)), do not have such exacting measurement precision requirements (Yver-Kwok et al., 2025; Chambers et al., 2025). Instruments for these purposes, however, would benefit from traceable calibration and improved portability. Furthermore, since atmospheric transport and dilution are significant drivers of indoor and outdoor radon concentration variability, the temporal resolution of detectors needs to remain capable of resolving mixing timescales of the atmospheric boundary layer (i.e. ≈1 h). To satisfy these needs, as part of the EMPIR project traceRadon, ANSTO and PTB collaborated on the design and construction of a portable two-filter dual flow-loop radon detector that could be traceably calibrated, with the goal of achieving

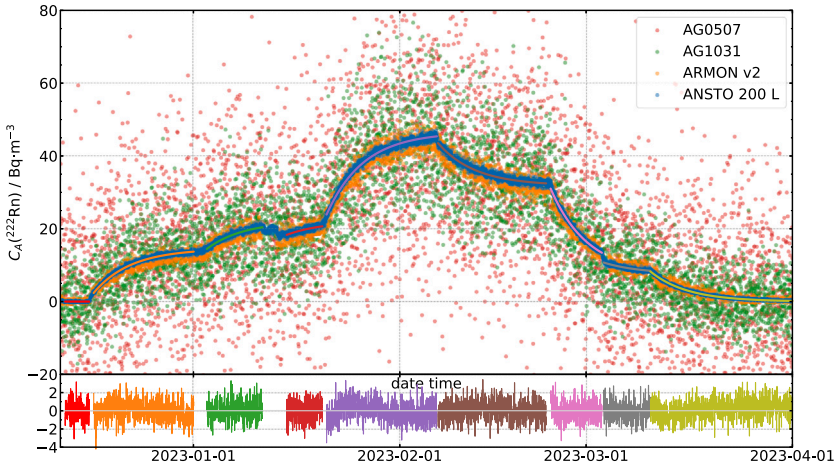

Fig. 2. Calibration measurement carried out in the controlled climate chamber at PTB. The upper part shows the calibrated measurements taken with different detectors in the calibration volume of about 21 m^3. These detectors were two AlphaGUARD (AG0507 (red points) - older device with larger background count rate, AG1031 (green points)), the ARMON v2 (orange points) and the ANSTO 200 L (blue points). The coloured lines show the calculated ^{222}Rn activity concentration using the emanation of the sources and the volume of the climate chamber which where determined traceable to the national standards of PTB and therefore traceable to the SI. Three different sources in different combinations have been used. Each combination of sources is shown with the different colours of the lines. The lower part of the picture shows, in the respective colours, the relative residuals between the measurement given by the ANSTO 200 L detector and the respective calibration value determined from the source combination and the time.

a total measurement uncertainty of 10% at an atmospheric radon concentration of 1 Bq m^{-3} (Röttger et al., 2021).

The ANSTO 200 L radon detector developed (Chambers et al., 2022) is 1.65 m tall, fits within a standard 19" instrument rack (spatial footprint 0.48 ·0.48 m^2), and – due to its durable marine grade stainless steel construction – weighs ≈80 kg. Its sampling flow rate is 10 L min^{-1}–14 L min^{-1}, and its counting uncertainty is designed to reach 30% at a radon activity concentration of 0.16 Bq m^{-3}. However, its two-piece design and small spatial footprint facilitated traceable calibration within the PTB controlled climate chamber (Röttger et al., 2023). Since this design of two-filter detector can be readily transported in a standard vehicle it is suited to be used as a Calibration Transfer Device at various observation network sites (e.g. ICOS, WMO GAW) (Schmithüsen et al., 2017; Grossi et al., 2020). However, the versatility and utility of this detector could be further improved by the development of a traceable in-situ operando calibration procedure.

Two-filter dual flow-loop detectors are so named because they have 2 flow loops (a sampling flow loop and an internal flow loop) and two filters (one filter to remove ambient radon progeny, a second filter to capture new radon progeny formed under controlled conditions). In this way, they respond directly (and entirely) to ambient activity concentrations of radon gas, not ambient progeny, and are therefore independent of disequilibrium or aerosol loss/removal effects.

Inside the main mixing volume, a small fraction of the sampled ^{222}Rn decays during the detector's 15 min–20 min flushing time. In the otherwise aerosol-free environment, the newly formed progeny remain unattached and charged. The specific progeny of interest are ^{218}Po and ^{214}Po.

To minimize decay loss of ^{218}Po ($T_{1/2}(^{218}\text{Po})$ = 184.3(13) s), the air inside the 200 L mixing volume needs to be rapidly circulated through the detector's second filter in the "measurement head". Consequently, the internal (second) flow loop usually operates at least an order of magnitude faster than the sampling flow rate.

To minimize plate-out loss of the unattached radon progeny within the detector, the internal flow loop blower is separated from the rest of the mixing volume by a cotton flow homogenizing screen, resulting in an approximation of laminar "plug flow" along the length of the detector to the measurement head.

Inside the measurement head the air passes through a 20 μm stainless steel mesh filter. Although the mesh size far exceeds that of the aerosol progeny, since they are charged and unattached, the filter has a high capture efficiency. The comparatively large mesh size also offers minimal flow impedance.

The mesh filter surrounds a 1.3 L volume (diameter = 12.5 cm) that is lined by clear plastic impregnated with silver activated zinc sulphide (ZnS). The average distance of the mesh to the ZnS is ≈4 mm. A consistent fraction of the α-particles released through the decay of captured ^{218}Po and ^{214}Po impact the ZnS and fluoresce, and the resulting photons are counted using a photomultiplier tube. Air temperature, relative humidity and pressure are measured directly inside the detector to enable STP and dry air mole fraction corrections of radon concentrations.

2.2. ARMON v2

The ARMON v2, developed at the Institute of energy Technologies (INTE) of the Technical University of Catalonia (UPC) (Grossi et al., 2012; Vargas et al., 2015) and now produced and maintained by Radonova, is a detector able to measure ambient atmospheric radon activity concentration of air sampled at a flow rate of 1.5 L min^{-1} within a spherical detection volume of a 20 L. Before reaching the active detector volume, the air flow passes a drying unit to reduce water vapour, a ^{220}Rn delay volume to remove ^{220}Rn and a filter to remove aerosols and progeny. The ARMON v2 consists of a 128 ·50 ·50 cm^3 box. Inlet and outlet air sampling connectors are located on the backside of the box. Details are found in Curcoll et al. (2024). The instrument function is based on a physical principle involving the collection of positively charged ^{218}Po and ^{214}Po ions, which are produced through the α-decay of ^{222}Rn within the detection chamber. A high voltage power supply provides a potential of 10 kV between a passive implanted planar silicon (PIPS) detector, located in the upper part of the sphere, and the sphere walls creating an electrostatic field which is used to collect the decay products of ^{222}Rn in the form of the positive ions of ^{218}Po, ^{214}Po or ^{210}Po on the surface of the PIPS detector. The radon activity concentration is determined by α-spectrometry of the α-particles emitted from these positive ions due to the ^{222}Rn decay within the detection volume. A pre-amplifier and a shaping-amplifier are then used to amplify and shape the electric signal in a Gaussian function in order to be read by a multichannel analyser (MCA) that transforms it into counts for specific energy bins.

This approach enables the clear identification of ^{218}Po (with a main α-emission-energy of 6002.35(9) keV) in the spectrum, distinguishing it

from other ^{222}Rn decay products such as ^{214}Po (7686.82(6) keV) and ^{210}Po (5304.33(7) keV).

Within the detection chamber, charged ^{218}Po ions can undergo neutralization through interactions with water vapour present in the sampled air, primarily via the formation of hydroxyl radicals (OH) (Hopke, 1989). To ensure optimal collection efficiency, it is crucial to minimize the concentration of water vapour within the detection volume. Additionally, the monitor's response must be adjusted to account for variations in humidity levels. The ARMON v2 instrument also includes flow rate, temperature and absolute humidity meters recorded by a data logger.

3. Calibration in stable atmospheres

The readings provided by the ^{222}Rn detectors where modelled by a piecewise function, consisting of either an ingrowing or a decaying exponential function, depending on the regime, which was regressed by a non-linear least-squares procedure. In this way, for each source (or combination of sources) installed in the experimental setup, the reading of the detectors is determined by extrapolation to the steady-state value.

Additionally, a background value was added to the model which accounts for both the zero-value indication background of the detector (due to ^{210}Po contamination) and the fact that some residual ^{222}Rn was experienced to be present in the chamber, which might be caused by the detector device itself, exhaling minimal amounts of ^{222}Rn, due to trace ^{226}Ra contamination in the materials used for construction of the detector. From the experimental data, the background reading of detectors per 30 min in the climate chamber are determined. The presence of an additional ^{222}Rn source in the chamber was checked by streaming aged synthetic air through the chamber (with its outlet open) over a course of 15 h such that the differential pressure between the chamber and the ambient pressure was stabilized at 200 Pa (setpoint controlled). A total of $\approx$15 m^3 of synthetic air were streamed through the chamber in this way.

The evolution of the detectors response during the time of calibration is depicted in Fig. 2. Due to experimental limitations, it was not feasible to entirely flush the climate chamber with synthetic air, since the required amounts of air were deemed to be too high to entirely replace the chamber air several times. It should be noted, however, that this effect does not impact the determination of the sensitivity of the detectors, since it only results in a constant offset on the intercept of a linear relationship between the device indication and the calculated ^{222}Rn activity concentration in the chamber. The parameters of this linear relationship were determined by linear least-squares, also accounting for the uncertainty in the independent variable (the activity concentration in the chamber) by utilizing orthogonal distance regression (ODR) as implemented in SciPy (Virtanen et al., 2020). The results of this procedure are given in the following Section 3.1, 3.2.

3.1. Static results for ANSTO 200 L

The result of the procedure described in Section 3 for the ANSTO 200 L detector is given in Fig. 3, and yields a sensitivity of 0.0380(6) m^3 s^{-1} Bq^{-1} (relative standard uncertainty of 2%) and an intercept of −22(16) (30 ·min)$^{-1}$. The scattering of the measurement results around the linear model from ODR have a relative standard deviation of 2.8%.

3.2. Static results for ARMON v2

The result of the procedure described in Section 3 for the ARMON v2 detector is given in Fig. 4, and yields a sensitivity of 0.0059(4) m^3 s^{-1} Bq^{-1} (relative standard uncertainty of 6.8%) and an intercept of 3(12) (30 ·min)$^{-1}$. The scattering of the measurement results around the linear model from ODR have a relative standard deviation of 2.2%.

4. Calibration in-situ operando/pulse calibration method

While the previously described method of static calibration seems to offer a straight forward way for calibration, it implies two important factors. First of all, the method only allows for application in a reference volume that is several times larger than the detector's active volume within which the detector in question can fit. For measurement devices intended for permanent outdoor use, like the ANSTO 1500 L ^{222}Rn detector, this is a severe limitation in practice, since calibration requires measurements to be suspended while the detector in question is packed down and shipped (at considerable cost) to a suitably equipped calibration facility (Chambers et al., 2025). While still possible for the ANSTO 200 L and ARMON v2 detectors, this is not practicable for the larger models like the ANSTO 1500 L detector, which are currently in routine operation at many sites across Europe. Furthermore, calibration factors may correlate with environmental parameters, and it is a very time consuming endeavour and experimentally difficult to assess every combination of environmental parameters the detector in question may experience during its operation in the field.

On the other hand, the specific design of the ANSTO 200 L and ARMON v2 detectors, as well as any other detector that relies on sampling air and measuring ^{222}Rn progeny, as e.g. the Heidelberg Radon Monitor (Levin et al., 2002), has a temporal response characteristic that does not need to be assessed under static calibration conditions. Specifically, the fact that the ANSTO device measures the ^{222}Rn progeny ^{218}Po and ^{214}Po that are accumulated onto a filter by sampling outdoor air with a certain flow-rate leads to a deviation of the temporal response from the actual outdoor ^{222}Rn concentration in question. This is due to the time required for the decay of intermediate ^{214}Bi and ^{214}Pb and that the concentration of ^{222}Rn inside the active volume does not equal the outdoor concentration at every instantaneous moment in time due to the sampling, especially in response to steep temporal gradients of the outdoor concentration. Applications of ^{222}Rn-based methods in the environmental sciences are, however, often concerned with its temporal evolution. Outdoor ^{222}Rn concentrations show a diurnal cycle correlated with vertical mixing in the atmosphere with a typical strong drop of outdoor ^{222}Rn concentrations following the onset of vertical mixing in the mornings after a time of nocturnal stability and correspondingly high ^{222}Rn concentration, Griffiths et al. (2016), Desideri et al. (2006) among others. This effect can be used in atmospheric studies, e.g. in Perrino et al. (2001), Williams et al. (2013, 2016), Chambers et al. (2019a,b) among others.

The device's signal is therefore given by a convolution of the actual ^{222}Rn concentration, and this has been addressed previously by the manufacturers using numerical deconvolution techniques (Griffiths et al., 2016). Such a method requires, however, that the kernel function of this convolution operation is known. In the following, an outline and specific results of a previously unreported method of calibration by using a pulse of ^{222}Rn of known activity that is directly injected into the inflow air-stream of such a device is given, which may also be applied to both in-field calibration and to assessment of the temporal response behaviour (Mertes, 2023b). In practice, this is realized by placing an emanation source inside a small, hermetically sealed volume such that it acts as a ^{222}Rn integration volume. After a certain ingrowth time, the ingrown and known activity of ^{222}Rn is injected by passing a stream of aged, synthetic air through this volume and into the detector's active volume, at a flow rate that ensures quick flushing of the integration volume. The ANSTO 200 L radon detector readings in response to such an input are shown in Fig. 5. The readings evaluated for the ARMON v2 detector are shown in Fig. 10.

Through a numerical model, the resultant response characteristics may be related to the initial ^{222}Rn activity and hence, both a calibration factor and the temporal response properties of such a device may be assessed. For comparison with the results from the static calibration, here, the focus is on deriving an equivalent, effective efficiency ε

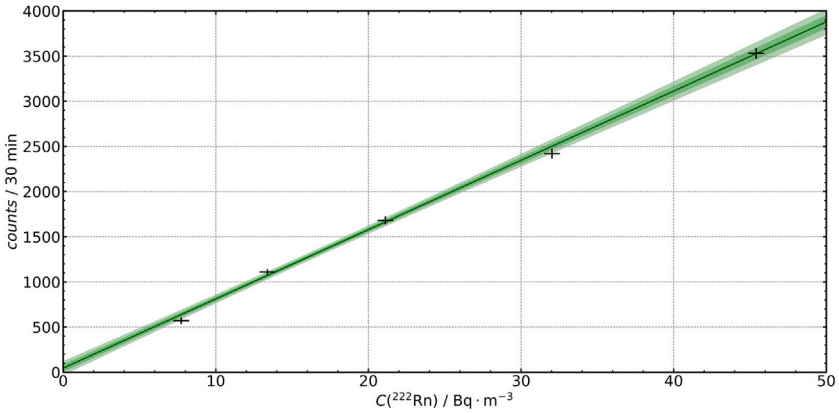

Fig. 3. Evaluation of a calibration measurement with the ANSTO 200 L detector in the PTB climate chamber. Three different ion implanted ^{222}Rn emanation sources have been used in different combinations to achieve 5 calibration points with different activity concentrations. The ANSTO 200 L ^{222}Rn activity concentration detector readings are depicted in black. The green curve represents the calibration curve determined by orthogonal distance regression and the 1 σ and 2 σ uncertainty (in different shades of green).

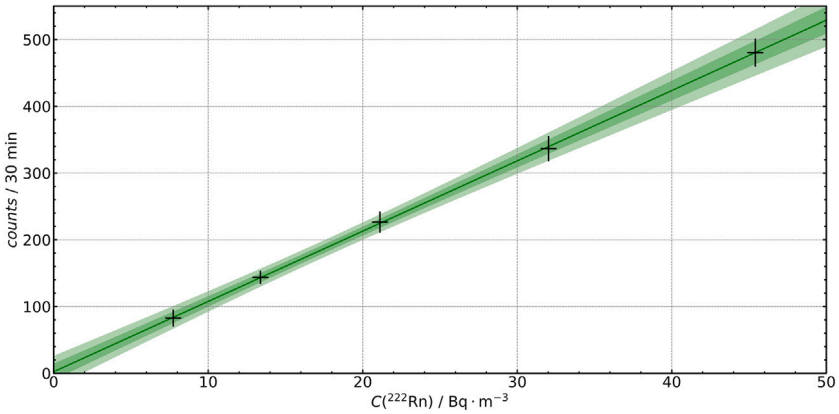

Fig. 4. Evaluation of a calibration measurement with the ARMON v2 detector in the PTB climate chamber. Three different ion implanted ^{222}Rn emanation sources have been used in different combinations to achieve 5 calibration points with different activity concentrations. The ARMON v2 ^{222}Rn activity concentration detector readings are depicted in black. The green curve represents the calibration curve determined by orthogonal distance regression and the 1 σ and 2 σ uncertainty (in different shades of green).

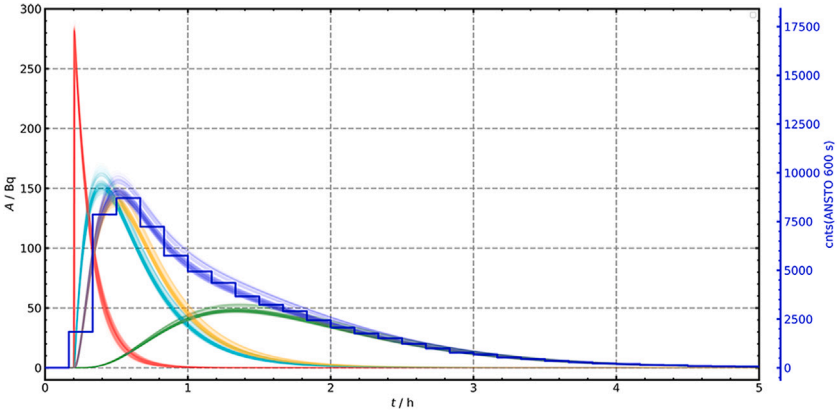

Fig. 5. Observed response of the ANSTO 200 L ^{222}Rn detector to an approximately Dirac Delta input of 284(3) Bq of ^{222}Rn (black axis on the left) and modelled activities of each nuclide (coloured) as computed from individual samples from the posterior distribution. In red the development of the ^{222}Rn activity in the delay volume of the detector. In turquoise for the ^{222}Rn activity in the active detector volume. In yellow for the ^{218}Po activity in the active detector volume. In green for the ^{214}Po activity in the active detector volume. In blue for the sum of ^{218}Po and ^{214}Po activity in the active detector volume, as it is detected by the ANSTO 200 L detector operation principle. The blue step curve represents the counts of the ANSTO 200 L detector recorded in 600 s intervals and scaled with the right hand y-axis scale. A good agreement with the shape of the theoretical curve of the sum of the ^{218}Po and ^{214}Po activity (blue curve) is observed.

or calibration factor. This technique relies on a theoretical model of the detector, which is found in Griffiths et al. (2016), and, which is related to the model reported in Mertes (2023b) and extended to the ARMON v2 here.

Therefore a state vector describing the state of the ^{222}Rn detector is chosen as

$$\boldsymbol{x} = \begin{bmatrix} A_{^{214}\mathrm{Po}} & A_{^{214}\mathrm{Bi}} & A_{^{214}\mathrm{Pb}} & A_{^{218}\mathrm{Po}} & A_{^{222}\mathrm{Rn,V_a}} & A_{^{222}\mathrm{Rn,V_d}} \end{bmatrix}^T. \tag{1}$$

It is assumed, that air is drawn into the delay volume V_d and across to the active volume V_a by a certain flow-rate Q. Any short-lived progeny (SLP) that enters V_d is removed by passage through a particulate filter and any SLP that is generated by the decay of ^{222}Rn within V_a is measured by the detection principle. In the experimental setup, Q is controlled by a calibrated mass-flow-controller (MFC) and set to the value that is standard for the sampling of the respective detector e.g. 10 L min^{-1} for the ANSTO 200 L and 1.5 L min^{-1} for the ARMON v2 with a standard uncertainty of 0.25% for e.g. a high precision, high-end thermal gas mass flow controller (Bronkhorst, 2026). Assuming instantaneous mixing and hence volumetric homogeneity of activity within the volumes V_d and V_a, the evolution of the state may be approximately described as

$$\frac{d\boldsymbol{x}}{dt} = \begin{bmatrix} -\lambda_{^{214}\mathrm{Po}} & \lambda_{^{214}\mathrm{Po}} & 0 & 0 & 0 & 0 \\ 0 & -\lambda_{^{214}\mathrm{Bi}} & \lambda_{^{214}\mathrm{Bi}} & 0 & 0 & 0 \\ 0 & 0 & -\lambda_{^{214}\mathrm{Pb}} & \lambda_{^{214}\mathrm{Pb}} & 0 & 0 \\ 0 & 0 & 0 & -\lambda_{^{218}\mathrm{Po}} & \lambda_{^{218}\mathrm{Po}} & 0 \\ 0 & 0 & 0 & 0 & -\lambda_{^{222}\mathrm{Rn}} - \frac{Q}{V_a} & \frac{Q}{V_d} \\ 0 & 0 & 0 & 0 & 0 & -\lambda_{^{222}\mathrm{Rn}} - \frac{Q}{V_d} \end{bmatrix} \boldsymbol{x} = \boldsymbol{F}\boldsymbol{x} \tag{2}$$

The solution is given as an initial value problem in terms of the matrix exponential and a convolution integral in case of an inhomogeneous term, i.e. an injection of ^{222}Rn into the delay volume which is acting as an input term on $A_{^{222}\mathrm{Rn,V_d}}$.

Either ^{218}Po, ^{214}Po or both are measured, depending on the detector. In case of the ANSTO 200 L, a combined signal of ^{218}Po and ^{214}Po is measured, whereas the ARMON v2 allows to spectrometrically differentiate between these isotopes. It is assumed, that the detector measures only the activities of ^{214}Po and ^{218}Po with distinct counting efficiencies of $\varepsilon_{^{214}\mathrm{Po}}$ and $\varepsilon_{^{218}\mathrm{Po}}$. This measurement is understood as being related to the time integrated state with an integration time of r, here chosen to be 600 s. Hence, the detector measurements are related to the state vector by

$$\boldsymbol{y}_t = \boldsymbol{H} \int_t^{t+r} \boldsymbol{x}(\tau)\mathrm{d}\tau \tag{3}$$

where, in case of the ANSTO 200 L,

$$\boldsymbol{H} = \begin{bmatrix} \varepsilon_{^{214}\mathrm{Po}} & 0 & 0 & \varepsilon_{^{218}\mathrm{Po}} & 0 & 0 \end{bmatrix} \tag{4}$$

and in case of the ARMON v2,

$$\boldsymbol{H} = \begin{bmatrix} \varepsilon_{^{214}\mathrm{Po}} & 0 & 0 & 0 & 0 & 0 \\ 0 & 0 & 0 & \varepsilon_{^{218}\mathrm{Po}} & 0 & 0 \end{bmatrix}. \tag{5}$$

When a pulse described by a Dirac-Delta distribution of area A_i, centred on time t_i, is injected into the air stream of the delay volume V_d, the resultant state may thus be modelled as

$$\boldsymbol{x}(t) = \begin{cases} 0 \cdot \boldsymbol{L} & t < t_i \\ e^{\boldsymbol{F}(t-t_i)} A_i \boldsymbol{L} & t \geq t_i \end{cases} \tag{6}$$

where $\boldsymbol{L} = \begin{bmatrix} 0 & 0 & 0 & 0 & 0 & 1 \end{bmatrix}^T$.

And thus, $\boldsymbol{y}_t$ can be evaluated as the piecewise function

$$\boldsymbol{y}_t = \begin{cases} b & t, t+r < t_i \\ b + \boldsymbol{H} \int_{t_i}^{t+r} e^{\boldsymbol{F}\tau} A_i \boldsymbol{L} d\tau & t < t_i, t+r \geq t_i \\ b + \boldsymbol{H} \int_{t}^{t+r} e^{\boldsymbol{F}\tau} A_i \boldsymbol{L} d\tau & t \geq t_i \end{cases} \tag{7}$$

where b signifies a certain background signal observed over the respective integration time r.

The matrix exponential required for these calculations is evaluated using symbolic computation of the Eigenvalue decomposition of $\boldsymbol{F}$ and the following identities

$$\exp(\boldsymbol{F}t) = \boldsymbol{P}\exp(\boldsymbol{\Lambda}t)\boldsymbol{P}^{-1} \tag{8}$$

where $\boldsymbol{P}$ signifies the stacked Eigenvectors and $\boldsymbol{\Lambda}$ signifies the diagonal matrix of corresponding Eigenvalues of $\boldsymbol{F}$ and

$$\int_a^b \exp\left(\boldsymbol{F}(\tau - c)\right) d\tau = \boldsymbol{P}\left(\exp(\boldsymbol{\Lambda}(b-c)) - \exp(\boldsymbol{\Lambda}(a-c))\right)\boldsymbol{\Lambda}^{-1}\boldsymbol{P}^{-1} \tag{9}$$

for the non-singular $\boldsymbol{F}$.

$\boldsymbol{y}_t$ corresponds to a counting process, and hence, the actual observed counts $\hat{\boldsymbol{y}}_t$ under knowledge of all parameters, signified by a parameter vector $\boldsymbol{\theta}$, are modelled by a Poisson distribution

$$\hat{\boldsymbol{y}}_t \mid \boldsymbol{\theta} \sim \mathrm{Poisson}(\boldsymbol{y}_t) \tag{10}$$

In such a model, the interest lies in simultaneously determining the counting efficiencies $\varepsilon_{^{218}\mathrm{Po}}$ and $\varepsilon_{^{214}\mathrm{Po}}$, such that they may be used to compute the effective steady state efficiency ε relatable to static calibration results as in case of the ANSTO 200 L

$$\varepsilon = (\varepsilon_{^{214}\mathrm{Po}} + \varepsilon_{^{218}\mathrm{Po}}) \cdot V_a \tag{11}$$

and in case of the ARMON v2 where only the ^{218}Po is evaluated

$$\varepsilon = \varepsilon_{^{218}\mathrm{Po}} \cdot V_a \tag{12}$$

keeping also in mind, that V_d and V_a are both not precisely known, but may be estimated from the respective geometrical dimensions of the device. However, it is possible to determine these using this modelling approach together with the detection efficiency. One may observe, that the specific observed shape of the sequence $\hat{\boldsymbol{y}}_t$ is a function of the relationships between the parameters V_d, V_a and $\varepsilon_{^{214}\mathrm{Po}}$, $\varepsilon_{^{218}\mathrm{Po}}$ and the not infinitely well determined input point t_i. In practice, observing a specific shape of $\hat{\boldsymbol{y}}_t$ (Figs. 5 and 10) thus only offers limited information on V_a and V_d, and therefore, these two parameters are poorly identifiable without additional prior information. Moreover, uncertainties of the decay constants λ_i and flow-rate Q propagate non-linearly across the model. The estimation of the resultant uncertainty in the derived quantity ε is therefore not straight-forward.

The way that was chosen to address both these factors lies in Bayesian analysis to estimate the resultant uncertainty in ε and to introduce prior distributions on V_a and V_d that are essential for convergence of this model into a physically reasonable result. As described above, the model suffers from poor identifiability under flat (i.e. improper) priors, due to the strong correlation of V_a, V_d, t_i and the efficiencies. The probability distribution of the full parameter vector $\boldsymbol{\theta}$ in light of the observed data $\hat{\boldsymbol{y}}_t$ time-series is of interest in order to quantify the resultant uncertainty and is given by Bayes theorem (omitting normalization) as

$$p(\boldsymbol{\theta} \mid \hat{\boldsymbol{y}}_t) \propto p(\hat{\boldsymbol{y}}_t \mid \boldsymbol{\theta}) p(\boldsymbol{\theta}) \tag{13}$$

where $p(\hat{\boldsymbol{y}}_t \mid \boldsymbol{\theta})$ is referred to as the likelihood given by Eq. (10) and $p(\boldsymbol{\theta})$ signifies the prior distribution of the parameters.

Markov-Chain Monte-Carlo (MCMC) methods allow samples to be drawn from the probability distribution $p(\boldsymbol{\theta}|\hat{\boldsymbol{y}}_t)$, the posterior, given that it can be evaluated, such as the Metropolis–Hastings (Hastings, 1970) algorithm and more recently, derivates of Hamiltonian Monte-Carlo. In the specific implementation used herein, the Hamiltonian Monte-Carlo method given by the efficient No-U-Turn-Sampler (NUTS) (Hoffman and Gelman, 2011), as implemented in the Python framework PyMC3 (Salvatier et al., 2016), was used to draw samples from the full posterior distribution. Thereby, both the uncertainty of the efficiency as well as the correlation between all model parameters are accessible, and, more importantly, the propagated uncertainty of all

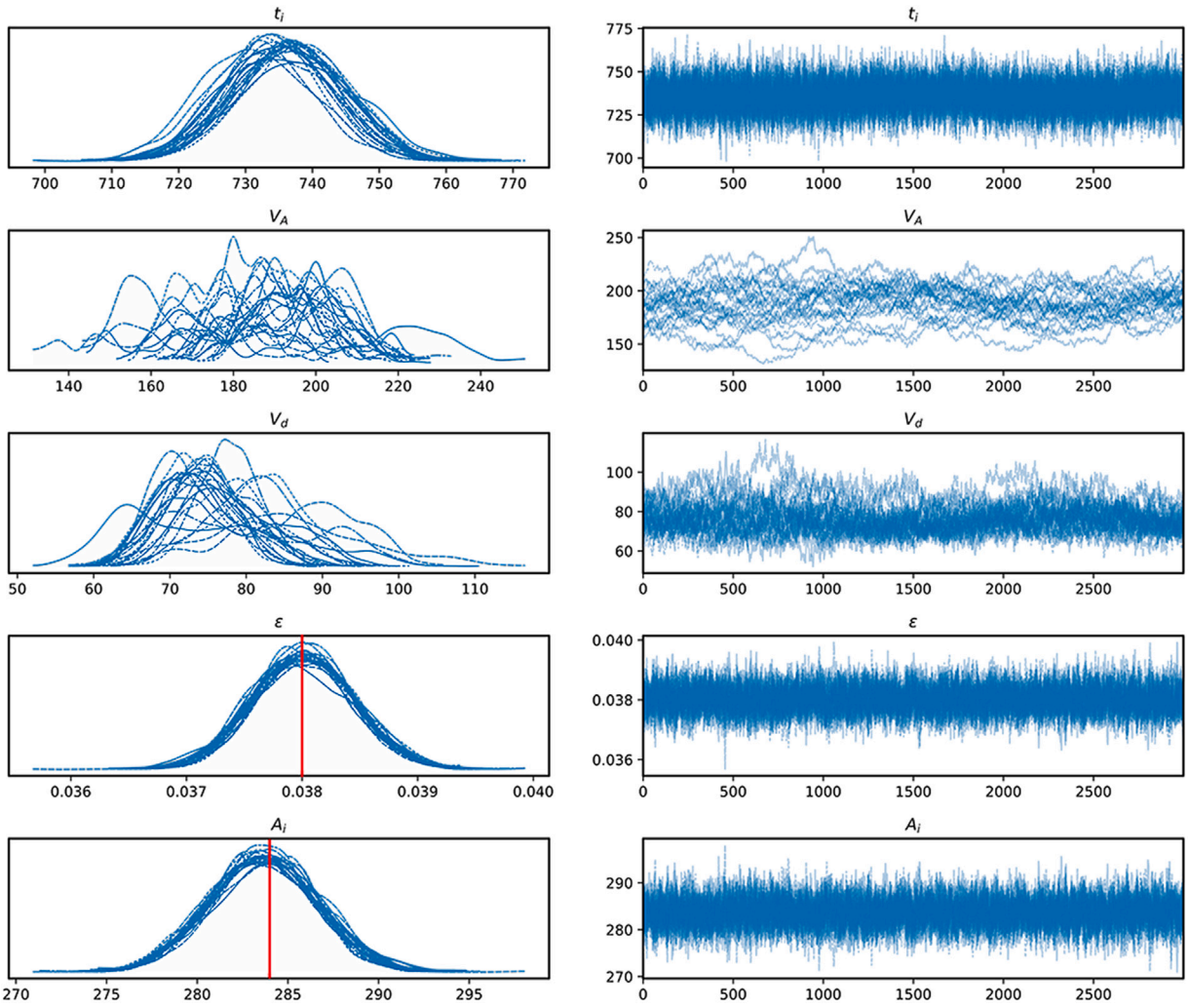

Fig. 6. Evaluation of a pulse calibration measurement with the ANSTO 200 L detector in the PTB climate chamber. Applying Markov-Chain Monte-Carlo allows the evolution to be followed during the sampling, which is shown here for the parameters: t_i, V_A, V_d, ε, A_i. It is obvious, that the efficiency ε is very stable and Gaussian distributed. The resulting efficiency ε is in excellent agreement with the static calibration result, which is indicated by the red bar in the PDF of ε. The model also respects the injected ^{222}Rn activity A_i (red bar, 284(3) Bq) and its uncertainty as seen in the PDF of A_i. The right hand figures are the evolution of the corresponding parameter with the number of Monte-Carlo run. The left hand figures are the histograms of the evolution of the corresponding parameters and give an indication of the stability and uncertainty distribution of it. For a detailed explanation of the figures refer to Salvatier et al. (2016).

input quantities on to ε may be assessed without additional simplifying assumptions such as the commonly applied truncated Taylor expansion (linearization).

V_d and V_a have been reparametrized to capture the fact that by construction $V_d < V_a$ as

$$V_a \sim \text{LogNormal} \tag{14}$$

$$z \sim \text{Beta} \tag{15}$$

$$V_d = z \cdot V_a \tag{16}$$

signifying, that V_a is given a LogNormal prior (with support only on $V_a > 0$) and introducing the auxiliary variable z with a Beta distribution (with support only on $0 < z < 1$) such that $V_a > V_d > 0$ is always fulfilled. These distributions have been parameterized such that they have reasonably high density at the crude approximations for the ANSTO 200 L of $V_a \approx 200\,\text{L}$ and $V_d \approx 50\,\text{L}$ and the ARMON v2 of $V_a \approx 20\,\text{L}$ and $V_d \approx 7\,\text{L}$, but do not introduce a lot of information. A prior PDF of model parameters is generated and used in the modelling of the response of the detector to an input of specified activity with unit Bq of ^{222}Rn, established from the implanted emanation source and for a fixed flow-rate. The pairwise correlations and marginal histograms of the full posterior from $5 \cdot 10^5$ samples drawn with the NUTS sampler are calculated and presented in the respective sections of the detectors 4.1 and 4.2 detailing the strong correlation between V_a and V_d. The uncertainty in the thus determined efficiency is almost entirely due to the uncertainty of the input ^{222}Rn activity, i.e., the emanation source. The modelling approach also allows the activity to be computed in each of the compartments of the detector (delay and active measurement volume) in response to the input activity and given its observations. These results may be utilized for deconvolution approaches in order to correct for the temporal response characteristics of this device.

4.1. Pulse results for ANSTO 200 L

The ANSTO 200 L was calibrated using the formalism described in Section 4. A ^{222}Rn activity was built up in a dedicated small Volume as shown in Fig. 1 (C) and was computed to have a total ^{222}Rn activity of 284(3) Bq at the time of application. The volume was directly connected to the inlet of the ANSTO 200 L and was flushed with aged synthetic air through the detector with a flow rate of 10.0000(25) L min^{-1} using a mass flow controller. During this pulse calibration period the sampling accumulation time of the ANSTO 200 L was set to 600 s

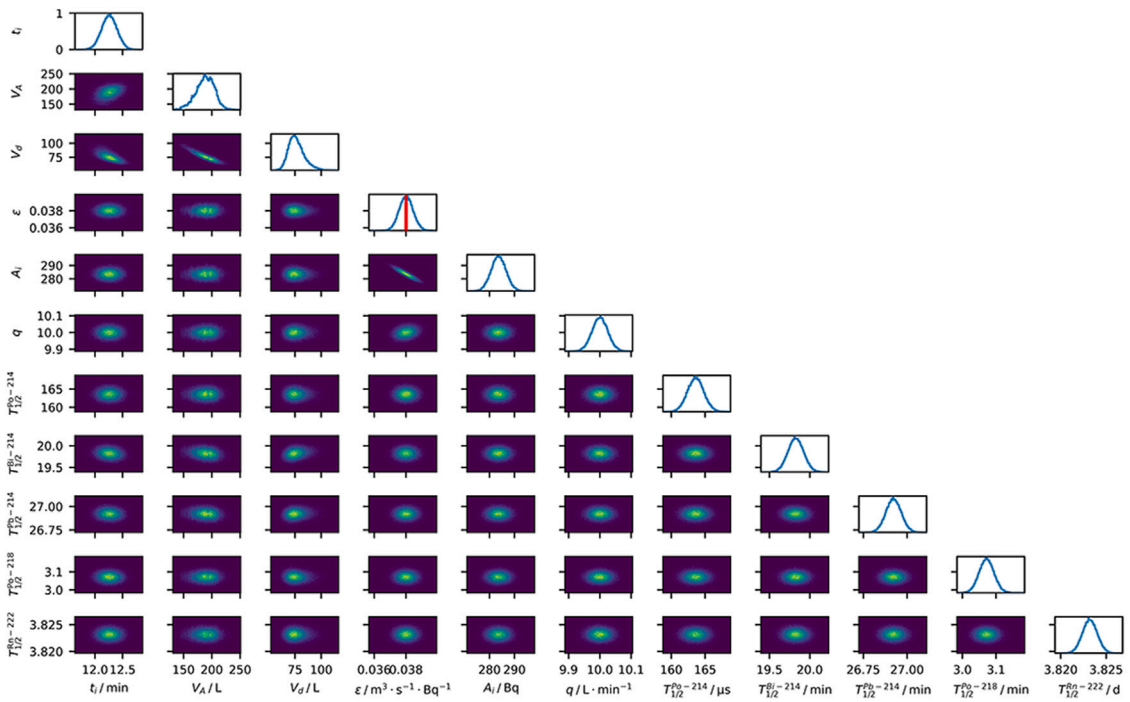

Fig. 7. Posterior distributions obtained from the pulsed calibration method for a 284(3) Bq pseudo Dirac-Delta input into the ANSTO 200 L ^{222}Rn detector at a flow rate of 10.0000(25) L min^{-1}. The red bar signifies the efficiency obtained from the static calibration method.

to achieve a better shape resolution for the temporal evolution. The measured response of the ANSTO 200 L to this input is shown in Fig. 5 as blue steps.

In Fig. 5 the measured results are compared with the prediction of the model for the different components and isotopes passing through the ANSTO 200 L. Details can be found in the caption of Fig. 5. Prior distributions were constructed from known input values (such as the decay constants) and the flow-rate and their uncertainties as described in Sections 2.1 and 2.2.

Applying the Markov-Chain Monte-Carlo allows for a detailed view on the evolution of the parameters with respect to the number of prior samples drawn in a chain. Fig. 6 shows some selected parameters and the evolution of their distributions. The correlation of V_a, V_d and t_i stems from the fact that different combinations of these parameters may essentially produce almost identical series of y_t and therefore, with almost identically assigned likelihood. The second last row, ε shows an uncorrelated trace and uncertainty of the desired result as the probability density function of the efficiency ε of the ANSTO 200 L detector. The red bar is indicating the result from the static calibration of the ANSTO 200 L. The last PDF A_i is shown to demonstrate that the prior input values and uncertainties are respected within this Markov-Chain Monte-Carlo simulation. This is how prior information assigned to physical quantities, such as the decay constants or the volumes, are incorporated into the model. The red bar in this case is the injected ^{222}Rn activity.

The final results for all parameters are given by the posterior distributions of samples which are shown in Fig. 7. The benign behaviour of all distributions is proof of a successful calculation. The red bar in the 4th row, 2D distribution is for comparison with the static calibration result. All the correlation plots show mostly independent/uncorrelated behaviour. V_d, V_a and t_i are correlated due to the reasons mentioned above. Additionally, the determined detection efficiency shows a strong correlation with the injected activity A_i. In the model, A_i influences epsilon linearly. Since the spread of epsilon is almost entirely caused by A_i, as indicated in the pairwise histogram in Fig. 7, the uncertainty in the determined efficiency is almost entirely due to the uncertainty of the input activity A_i and not due to other factors such as the counting statistics or the uncertainty of other parameters.

4.2. Pulse results for ARMON v2

Since the ARMON v2 by its detection principle is capable of retrieving energy resolved, thus spectrometric, information it is also possible to distinguish between the different α-particle emitting ^{222}Rn progeny. This feature is visible in Fig. 8 which shows an integral spectrum over the whole time of the pulse calibration. The number of recorded events as function of the channel is presented. The assignment of the different features (peaks) to the different progeny decays is given in Fig. 8 caption.

Since the integration time of the ARMON v2 was reduced to 60 s during the pulse calibration, temporally resolved information is also available. An overview of all this information, even though compressed in time and channels for better visibility, is given in Fig. 9.

Here as a colour coded 3D plot the evolution with time is given on the x-axis, the α-energy represented by the channels are given on the y-axis and the number of corresponding events are colour coded, plotted to the z-axis.

Projection of this diagram to the x-axis for the different regions determined from Fig. 8, allows for ^{222}Rn progeny separated readings of the ARMON v2. Fig. 10 displays these results as steps in blue for the ^{218}Po and in black for ^{214}Po.

As for the ANSTO 200 L the results of the model for the different compartments of the ARMON v2 detector and the different ^{222}Rn progeny are shown here in different colours as individual samples drawn from the posterior using the described Monte-Carlo methods. The details are explained in Fig. 10. The good agreement between the shapes from the model and the respective channel readings from the ARMON v2 measurements justify the described modelling approach.

The evolution of select parameters within several Markov-Chains of the Monte-Carlo simulation are given in Fig. 11, and show that convergence was achieved within each chain for the respective parameters.

Overall, the convergence behaviour of the parameters within the Markov-Chains are better in case of the ARMON v2 as compared to the

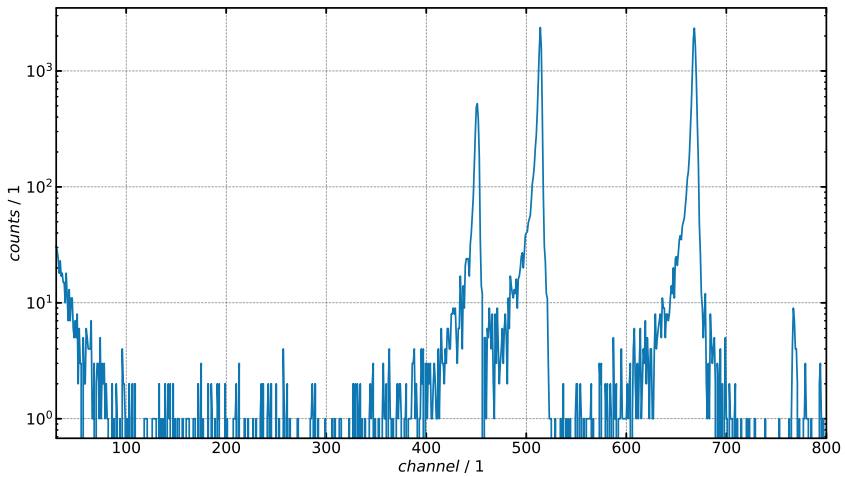

Fig. 8. Time integrated spectrum over the time the pulse calibration was performed with the ARMON v2 detector in the climate chamber of PTB. The integral counts per channel are shown as function of the respective channel, which is proportional to the α-energy. The two main peaks (> 10^3 counts) are the α-particles originating from the decay of ^{218}Po (channel 510, E_α = 6.11 MeV) and ^{214}Po (channel 660, E_α = 7.83 MeV). In this representation also visible is the peak generated by α-particles originating from the decay of ^{210}Po (channel 450, E_α = 5.41 MeV) which is not visible in Fig. 9 because it is evenly distributed over time during all the calibration time and due to the logarithmic scaling of the y-axis here.

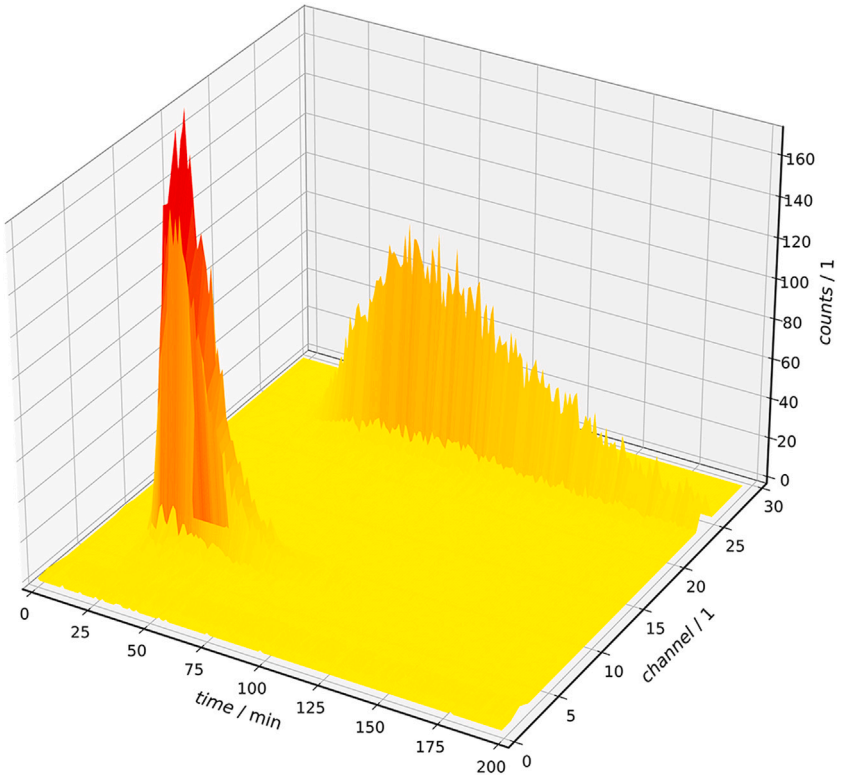

Fig. 9. 3D representation of a pulse calibration measurement with the ARMON v2 detector in the PTB climate chamber. As time evolution over the x-axis the integrated 60 s counts (z-axis) for grouped number of channels as y-axis are shown in a coloured contour plot. The two groups of distributions are clearly separated. The first building and faster decaying ^{218}Po with the lower channels and smaller times and the from the decay of the ^{218}Po formed ^{214}Po decays with later time and higher channels (α-energy). The respective regions of interest are used to evaluate the pulse calibration of the ARMON v2 for each isotope separately.

ANSTO 200 L. The correlation of V_a and V_d in the probability space poses a general difficulty for the entire exploration of the posterior distribution by the applied MCMC methods, since the step length for sampling is not uniform with each dimension in the probability space. It may be, that the additional information provided in the form of the nuclide specific measurements in case of the ARMON v2 alleviates this to a certain degree.

The overall results of the MCMC is presented in Fig. 12.

The features shown are comparable to Fig. 7 from the ANSTO 200 L. The strong correlation visible between the active detection volume V_a and the delay volume V_d, as well as between the injected activity A_i and the efficiency ε is due to the same reasons as given in Section 4.1. The comparison with the static calibration of the ARMON v2 is also indicated through the red bar. The uncertainty of the static calibration is indicated through the dotted red horizontal line and cannot be fully displayed in this figure.

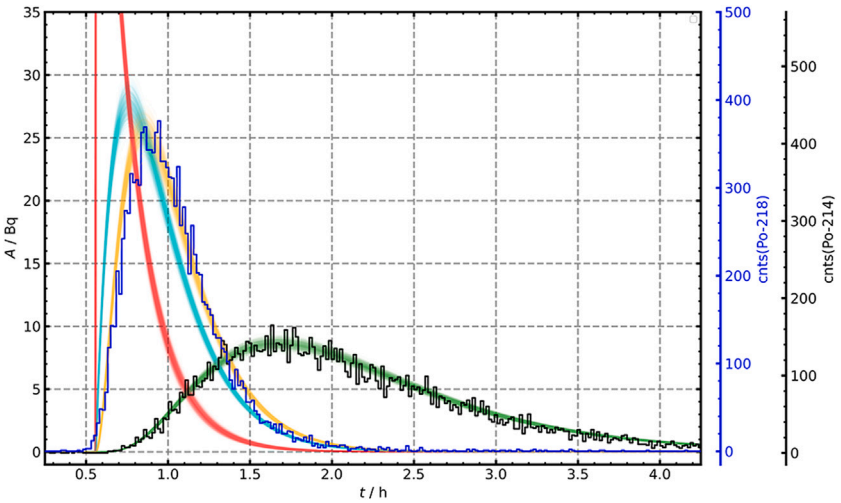

Fig. 10. Evaluation of a pulse calibration measurement with the ARMON v2 detector in the PTB climate chamber. Observed response of the ARMON v2 ^{222}Rn detector to a approximately Dirac Delta input of 53.9(11) Bq of ^{222}Rn (blue and black step function) and modelled activities of each nuclide (coloured) as computed from individual samples from the posterior distribution. In red the development of the ^{222}Rn activity in the delay volume of the detector. In turquoise for the ^{222}Rn activity in the active detector volume. In yellow for the ^{218}Po activity in the active detector volume. In green for the ^{214}Po activity in the active detector volume. The blue step curve represents the counts of the ARMON v2 detector recorded in 60 s intervals, identified as ^{218}Po decays and is scaled with the blue right hand *y*-axis scale. It is compared with the yellow curve for ^{218}Po model decays. The black step curve represents the counts of the ARMON v2 detector recorded in 60 s intervals, identified as ^{214}Po decays and is scaled with the black right hand *y*-axis scale. It is compared with the green curve for ^{214}Po model decays. A good agreement with the shape of the theoretical curves of the ^{218}Po and ^{214}Po activity (respectively yellow and green) is observed with the respective measured step functions (blue and black).

5. Comparison and uncertainty budget

In general it has to be stated, that an agreement between static calibration and pulse calibration is found within the uncertainties derived from the different methods. In general the activity (pulse calibration) or activity concentration (static calibration) was found to be the dominant part of the uncertainties. This is true for both, the ANSTO 200 L and the ARMON v2 detector, even though these detectors are operating on a physically and technically different basis. Different ^{222}Rn activities have been used since the two detectors have a difference of a factor of 10 in the active detection volume. The detailed results are found in following Sections 5.1 and 5.2.

5.1. Method comparison for ANSTO 200 L

The static calibration method for the ANSTO 200 L detector, performed at the PTB climate chamber for 5 different calibration points yielded a sensitivity of 0.0380(6) m^3 s^{-1} Bq^{-1} (relative standard uncertainty 2%) for calibrations points between 5 Bq $m^{-3}$and 50 Bq m^{-3}.

The pulse calibration method for the ANSTO 200 L detector also performed at PTB, injecting a pseudo delta Dirac pulse of 284(3) Bq of ^{222}Rn yield a sensitivity of 0.0380(4) m^3 s^{-1} Bq^{-1} (relative standard uncertainty 1%).

Both results are in perfect agreement.

5.2. Method comparison for ARMON v2

The static calibration method for the ARMON v2 detector, performed at the PTB climate chamber for 5 different calibration points yielded a sensitivity of 0.0059(4) m^3 s^{-1} Bq^{-1} (relative standard uncertainty 6.8%) for calibrations points between 5 Bq m^{-3} and 50 Bq m^{-3}.

The pulse calibration method for the ARMON v2 detector also performed at PTB, injecting a pseudo delta Dirac pulse of 53.9(11) Bq of ^{222}Rn yield a sensitivity of (.00557(10) m^3 s^{-1} Bq^{-1} (relative standard uncertainty 2%).

Both results are in very good agreement within the assigned standard uncertainties.

6. Summary, conclusions and outlook

Two research quality detectors, capable of measuring time resolved low-levels of outdoor air ^{222}Rn activity concentration have been characterized traceable to German national standards and therefore to the SI. Two completely different methods have been applied. A static calibration in the climate chamber of PTB that allows for background and stability testing as well as comparison of different devices. It is possible to carry out this calibration in the ^{222}Rn activity concentration range equal to the intended application of the detector but requires the detector to fit into the appropriate calibration chamber — which is not always the case. The calibrated detectors are intensively investigated and are therefore suitable as transfer device, which to transfer their calibration to detectors in place either in buildings or remote places for in-situ operando calibration transfer.

Since this calibration technique is time consuming, taking weeks to months, and restricted to at least portable detectors, a second new method is investigated and compared.

The pulse calibration method is applicable to active detectors. Active in the sense of active air sampling (not applicable at all to diffusive operated detectors or passive detectors) detectors with known operating principle and the possibility to access and control the direct readout of the detected signals. For these detectors a fast calibration can be carried out, outside of a calibration chamber, in place of operation and without interrupting the operation (in-situ operando). In both discussed cases the results of the pulse calibration was in agreement with the static calibration within the respective assigned uncertainty. This proves the new pulse calibration method is adequate for the calibration of even highly sensitive, research grade, low-level ^{222}Rn detectors. The time response of the detectors under normal operation condition is not derived from these measurements and should be addressed in future investigations.

The described procedure currently still makes use of synthetic air to have a ^{222}Rn free background for calibration with the pulse. Investigations are intended to test the application of AI based pattern recognition to perform repeated pulse calibration with environmental air, thus avoiding the need to have synthetic air available in place

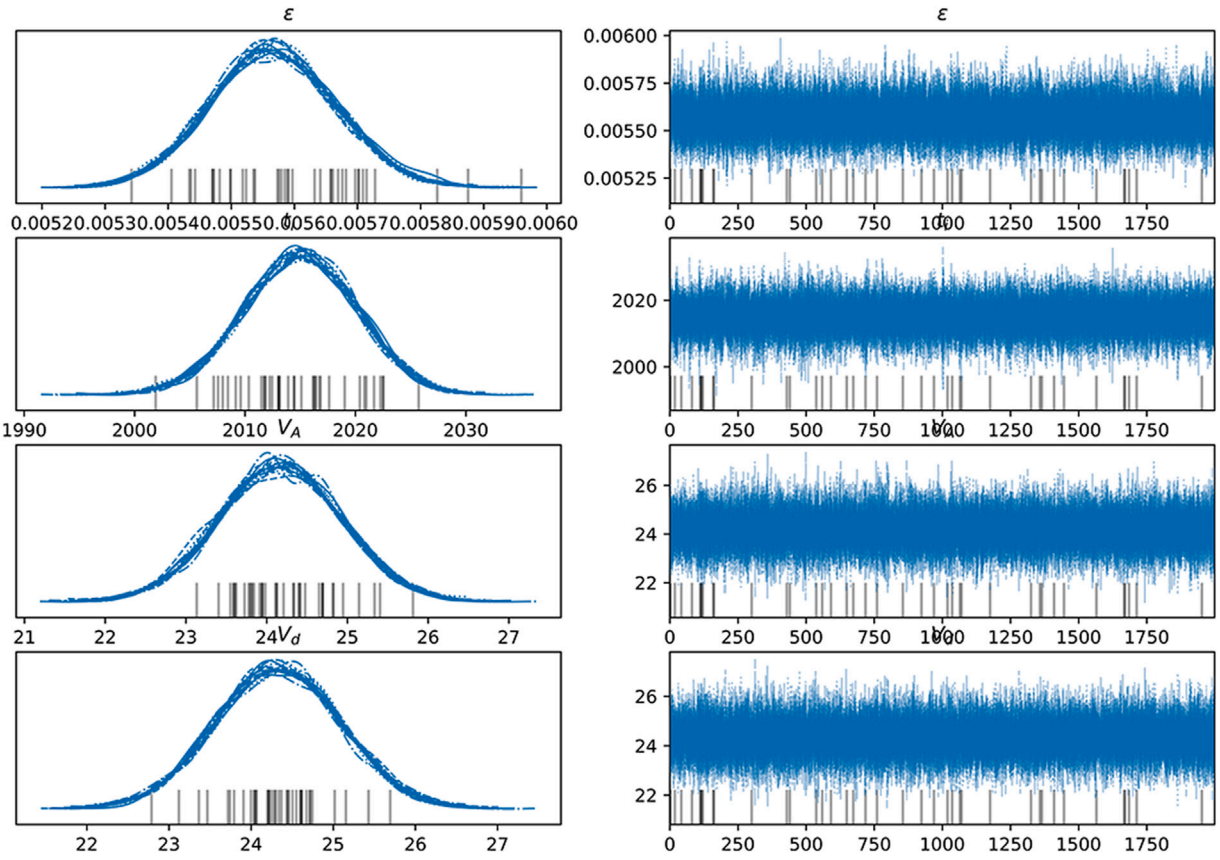

Fig. 11. Evaluation of a pulse calibration measurement with the ARMON v2 detector in the PTB climate chamber. Applying Markov-Chain Monte-Carlo allows the evolution to be followed during the sampling, which is shown here for the parameters: ε, t_i, V_A, V_d. It is obvious, that the Efficiency ε is very stable and Gaussian distributed, which proves the capability of this calibration and the resulting Efficiency ε is in agreement with the static calibration result. It also shows the reasonable results for the delay volume V_d and the active detector volume V_A. For the delay volume V_d the volume of the drying unit has to be taken into account, since it was in place during these experiments. In principle it could be omitted since the flushing is done with synthetic air which is free of humidity. Due to the fact, that more information from different decay time, because of the spectrometric information, is available, the distribution of the active volume V_A is nicely defined and properly distributed. The right hand figures are the evolution of the corresponding parameter with the number of Monte-Carlo run. The left hand figures are the histograms of the evolution of the corresponding parameters and give an indication of the stability and uncertainty distribution of it. For a detailed explanation of the figures refer to (Salvatier et al., 2016).

of calibration and allowing the detector's operation to continue uninterrupted. Another possibility is the sampling and compressing of air in-place and letting it age so that the ^{222}Rn decays instead of having to ship synthetic air.

CRediT authorship contribution statement

Stefan Röttger: Writing – review & editing, Writing – original draft, Visualization, Validation, Supervision, Software, Resources, Project administration, Methodology, Investigation, Funding acquisition, Formal analysis, Data curation, Conceptualization. **Florian Mertes:** Writing – review & editing, Writing – original draft, Visualization, Validation, Software, Methodology, Investigation, Formal analysis, Data curation. **Scott Chambers:** Writing – review & editing, Writing – original draft, Validation, Investigation, Data curation. **Alan Griffiths:** Writing – review & editing, Software, Methodology, Formal analysis. **Roger Curcoll:** Writing – review & editing, Data curation. **Arturo Vargas:** Writing – review & editing, Supervision, Resources, Data curation. **José Luis Gutiérrez Villanueva:** Writing – review & editing, Resources. **Annette Röttger:** Writing – review & editing, Writing – original draft, Validation, Project administration, Methodology, Investigation, Funding acquisition, Conceptualization.

Funding

The work presented here was carried out with the support of project funding which is:

- The project 19ENV01 traceRadon has received funding from the EMPIR programme, Germany co-financed by the Participating States and from the European Union's Horizon 2020 research and innovation programme.
- The project 23IND07 RadonNET has received funding from the European Partnership on Metrology, co-financed from the European Union's Horizon Europe Research and Innovation Programme and by the Participating States.
- The project NuClim has received funding from the European EURATOM programme co-financed by the Participating States and from the European Union's Horizon Europe research and innovation programme – EURATOM GAP 101166515.

Declaration of competing interest

The authors declare that they have no known competing financial interests or personal relationships that could have appeared to influence the work reported in this paper.

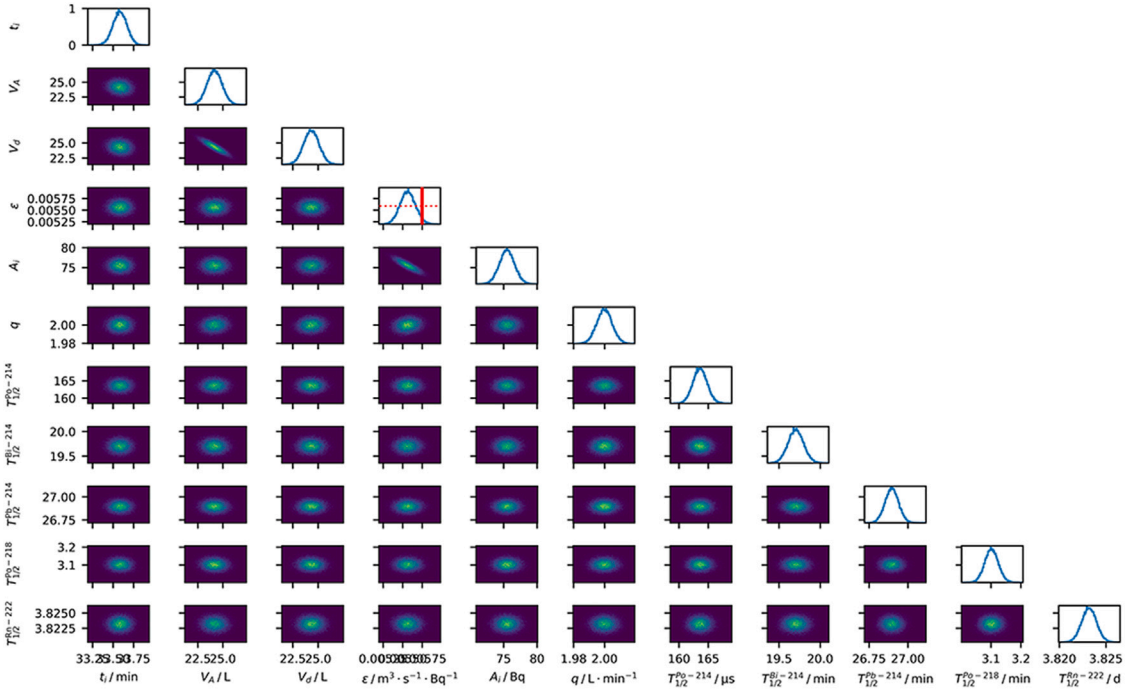

Fig. 12. Posterior distributions obtained from the pulse calibration method for a 53.9(11) Bq pseudo Dirac-Delta input into the ARMON v2 ^{222}Rn detector at a flow rate of 2.0000(25) L min^{-1}. The red vertical bar signifies the efficiency obtained from the static calibration method. The red dotted horizontal bar indicates the uncertainty range of the static calibration, which cannot be fully displayed in this figure.

Data availability

Data will be made available on request.

References

Bureau International des Poids et Measures, 2019. The International System of Units (SI). Technical Report, Bureau International des Poids et Measures, Sèvres, http://dx.doi.org/10.59161/AUEZ1291.

Bé, M.-M., Chisté, V., Dulieu, C., Browne, E., Chechev, V., Kuzmenko, N., Kondev, F., Luca, A., Galán, M., Pearce, A., Huang, X., 2008. Table of radionuclides. In: Monographie BIPM-5, vol. 4, Bureau International des Poids et Mesures, Pavillon de Breteuil, F-92310 Sèvres, France, URL: http://www.bipm.org/utils/common/pdf/monographieRI/Monographie_BIPM-5_Tables_Vol4.pdf.

Bronkhorst, 2026. High-end gas flow controller. URL: https://www.bronkhorst.com/products/gas-flow/el-flow-prestige/.

Chambers, S.D., Griffiths, A.D., Williams, A.G., Sisoutham, O., Morosh, V., Röttger, S., Mertes, F., Röttger, A., 2022. Portable two-filter dual-flow-loop ^{222}Rn detector: stand-alone monitor and calibration transfer device. Adv. Geosci. 57, 63–80. http://dx.doi.org/10.5194/adgeo-57-63-2022.

Chambers, S.D., Guérette, E.-A., Monk, K., Griffiths, A.D., Zhang, Y., Duc, H., Cope, M., Emmerson, K.M., Chang, L.T., Silver, J.D., Utembe, S., Crawford, J., Williams, A.G., Keywood, M., 2019b. Skill-testing chemical transport models across contrasting atmospheric mixing states using radon-222. Atmosphere 10, 25. http://dx.doi.org/10.3390/atmos10010025.

Chambers, S.D., Karstens, U., Griffiths, A.D., Röttger, S., Frumau, A., Roulston, C.T., Sperlich, P., Vogel, F., Podstawczyńska, A., Kikaj, D., Gachkivskyi, M., Ramonet, M., Mitrevski, B., Vaupotič, J., Chen, X., Röttger, A., 2025. Review of the Radon Tracer Method for GHG emission estimates: development, application guidelines, improvements, and caveats. http://dx.doi.org/10.5194/egusphere-2025-5042.

Chambers, S., Podstawczyńska, A., Pawlak, W., Fortuniak, K., Williams, A., Griffiths, A., 2019a. Characterizing the state of the urban surface layer using radon-222. J. Geophys. Res.: Atmospheres 124, 770–788. http://dx.doi.org/10.1029/2018JD029507.

Chambers, S.D., Williams, A.G., Conen, F., Griffiths, A.D., Reimann, S., Steinbacher, M., Krummel, P.B., Steele, L.P., van der Schoot, M.V., Galbally, I.E., Molloy, S.B., Barnes, J.E., 2016. Towards a universal "baseline" characterisation of air masses for high- and low-altitude observing stations using radon-222. Aerosol Air Qual. Res. 16, 885–899. http://dx.doi.org/10.4209/aaqr.2015.06.0391.

Curcoll, R., Grossi, C., Röttger, S., Vargas, A., 2024. Full characterization and calibration of a transfer standard monitor for atmospheric radon measurements. Atmospheric Meas. Tech. 17, 3047–3065. http://dx.doi.org/10.5194/amt-17-3047-2024.

Desideri, D., Roselli, C., Feduzi, L., Meli, M.A., 2006. Monitoring the atmospheric stability by using radon concentration measurements: A study in a central Italy site. J. Radioanal. Nucl. Chem. 270, 523–530. http://dx.doi.org/10.1007/s10967-006-0458-1.

Griffiths, A.D., Chambers, S.D., Williams, A.G., Werczynski, S., 2016. Increasing the accuracy and temporal resolution of two-filter radon–222 measurements by correcting for the instrument response. Atmospheric Meas. Tech. 9, 2689–2707. http://dx.doi.org/10.5194/amt-9-2689-2016.

Grossi, C., Arnold, D., Adame, J., López-Coto, I., Bolívar, J., de la Morena, B., Vargas, A., 2012. Atmospheric ^{222}Rn concentration and source term at El Arenosillo 100 m meteorological tower in southwest Spain. Radiat. Meas. 47, 149–162. http://dx.doi.org/10.1016/j.radmeas.2011.11.006.

Grossi, C., Chambers, S.D., Llido, O., Vogel, F.R., Kazan, V., Capuana, A., Werczynski, S., Curcoll, R., Delmotte, M., Vargas, A., Morguí, J.-A., Levin, I., Ramonet, M., 2020. Intercomparison study of atmospheric ^{222}Rn and ^{222}Rn progeny monitors. Atmospheric Meas. Tech. 13, 2241–2255. http://dx.doi.org/10.5194/amt-13-2241-2020.

Hastings, W.K., 1970. Monte Carlo sampling methods using Markov chains and their applications. Biometrika 57, 97–109. http://dx.doi.org/10.1093/biomet/57.1.97.

Hoffman, M.D., Gelman, A., 2011. The No-U-Turn Sampler: Adaptively setting path lengths in Hamiltonian Monte Carlo.

Honig, A., Paul, A., Röttger, S., Keyser, U., 1998. Environmental control of the German radon reference chamber. Nucl. Instruments Methods Phys. Res. Sect. A: Accel. Spectrometers, Detect. Assoc. Equip. 416 (2–3), 525–530. http://dx.doi.org/10.1016/S0168-9002(98)00788-8, URL: https://scispace.com/pdf/environmental-control-of-the-german-radon-reference-chamber-3gfay2wsht.pdf, https://linkinghub.elsevier.com/retrieve/pii/S0168900298007888.

Hopke, P.K., 1989. The initial behavior of ^{218}Po in indoor air. Environ. Int. 15, 299–308. http://dx.doi.org/10.1016/0160-4120(89)90042-1.

Levin, I., Born, M., Cuntz, M., Langendörfer, U., Mantsch, S., Naegler, T., Schmidt, M., Varlagin, A., Verclas, S., Wagenbach, D., 2002. Observations of atmospheric variability and soil exhalation rate of radon-222 at a Russian forest site: Technical approach and deployment for boundary layer studies. Tellus B: Chem. Phys. Meteorol. 54, 462. http://dx.doi.org/10.3402/tellusb.v54i5.16681.

Mertes, F., 2023a. Primary ^{222}Rn emanation standards for low-level applications. http://dx.doi.org/10.15488/15373, URL: https://repo.uni-hannover.de/handle/123456789/15493,

Mertes, F., 2023b. Primary ^{222}Rn emanation standards for low-level applications. URL: https://www.irs.uni-hannover.de/fileadmin/irs/Arbeiten/Doktor/drmertes.pdf.

Mertes, F., Kneip, N., Heinke, R., Kieck, T., Studer, D., Weber, F., Röttger, S., Röttger, A., Wendt, K., Walther, C., 2022. Ion implantation of ^{226}Ra for a primary ^{222}Rn emanation standard. Appl. Radiat. Isot. 181, http://dx.doi.org/10.1016/j.apradiso.2021.110093.

NuClim, 2023. EURAMET, Partnership on Metrology, Nuclear observations to improve Climate research and GHG emission estimates (NuClim). URL: https://NuClim.eu. (Accessed 18 June 2025).

Perrino, C., Pietrodangelo, A., Febo, A., 2001. An atmospheric stability index based on radon progeny measurements for the evaluation of primary urban pollution. Atmos. Environ. 35, 5235–5244. http://dx.doi.org/10.1016/S1352-2310(01)00349-1.

RadonNET, 2023. EURAMET, Partnership on Metrology, Radon metrology: Sensor networks for large buildings and future cities (RadonNET). URL: https://radon-network.eu. (Accessed 18 June 2025).

Röttger, A., Röttger, S., Grossi, C., Vargas, A., Curcoll, R., Otáhal, P., Hernández-Ceballos, M.Á., Cinelli, G., Chambers, S., Barbosa, S.A., Ioan, M.-R., Radulescu, I., Kikaj, D., Chung, E., Arnold, T., Yver-Kwok, C., Fuente, M., Mertes, F., Morosh, V., 2021. New metrology for radon at the environmental level. Meas. Sci. Technol. 32, 124008. http://dx.doi.org/10.1088/1361-6501/ac298d, URL: https://iopscience.iop.org/article/10.1088/1361-6501/ac298d.

Röttger, S., Röttger, A., Mertes, F., Morosch, V., Ballé, T., Chambers, S., 2023. Evolution of traceable radon emanation sources from MBq to few Bq. Appl. Radiat. Isot. 196, 110726. http://dx.doi.org/10.1016/j.apradiso.2023.110726.

Salvatier, J., Wiecki, T., Fonnesbeck, C., 2016. Probabilistic programming in Python using PyMC3. PeerJ Comput. Sci. 2 e55.

Schmithüsen, D., Chambers, S., Fischer, B., Gilge, S., Hatakka, J., Kazan, V., Neubert, R., Paatero, J., Ramonet, M., Schlosser, C., Schmid, S., Vermeulen, A., Levin, I., 2017. A European-wide ^{222}Rn and ^{222}Rn progeny comparison study. Atmospheric Meas. Tech. 10, 1299–1312. http://dx.doi.org/10.5194/amt-10-1299-2017.

traceRadon, 2019. EURAMET, EMPIR, Radon metrology for use in climate change observation and radiation protection at the environmental level (traceRadon). URL: http://traceradon-empir.eu. (Accessed 18 June 2025).

Vargas, A., Arnold, D., Adame, J., Grossi, C., Hernández-Ceballos, M., Bolivar, J., 2015. Analysis of the vertical radon structure at the Spanish "El Arenosillo" tower station. J. Environ. Radioact. 139, 1–17. http://dx.doi.org/10.1016/j.jenvrad.2014.09.018.

Virtanen, P., Gommers, R., Oliphant, T.E., Haberland, M., Reddy, T., Cournapeau, D., Burovski, E., Peterson, P., Weckesser, W., Bright, J., van der Walt, S.J., Brett, M., Wilson, J., Millman, K.J., Mayorov, N., Nelson, A.R.J., Jones, E., Kern, R., Larson, E., Carey, C.J., Polat, İ., Feng, Y., Moore, E.W., VanderPlas, J., Laxalde, D., Perktold, J., Cimrman, R., Henriksen, I., Quintero, E.A., Harris, C.R., Archibald, A.M., Ribeiro, A.H., Pedregosa, F., van Mulbregt, P., SciPy 1.0 Contributors, 2020. SciPy 1.0: Fundamental Algorithms for Scientific Computing in Python. Nature Methods 17, 261–272. http://dx.doi.org/10.1038/s41592-019-0686-2.

Williams, A.G., Chambers, S.D., Conen, F., Reimann, S., Hill, M., Griffiths, A.D., Crawford, J., 2016. Radon as a tracer of atmospheric influences on traffic-related air pollution in a small inland city. Tellus B: Chem. Phys. Meteorol. 68, 30967. http://dx.doi.org/10.3402/tellusb.v68.30967.

Williams, A., Chambers, S., Griffiths, A., 2013. Bulk mixing and decoupling of the nocturnal stable boundary layer characterized using a ubiquitous natural tracer. Bound.-Layer Meteorol. 149, 381–402. http://dx.doi.org/10.1007/s10546-013-9849-3.

Yver-Kwok, C., Ramonet, M., Rivier, L., Lian, J., Grossi, C., Curcoll, R., Kikaj, D., Chung, E., Karstens, U., 2025. Measurement report: Eight years of greenhouse gas fluxes at Saclay, France, estimated with the Radon Tracer Method. Atmospheric Chem. Phys. 25 (22), 16085–16106. http://dx.doi.org/10.5194/acp-25-16085-2025.